Macromolecules

pubs.acs.org/Macromolecules Article

Temperature-Dependent Structural Transition in Hydrogen-Bonded Supramolecular Polymers Using Coarse-Grained Simulations

Nengjie Cao, Fengxiang Zhou, Xianggui Zhou, Jinyuan Mao, Xiangmeng Jia, and Jiajia Zhou*

Cite This: *Macromolecules* 2026, 59, 1517−1528

Read Online

ACCESS | Metrics & More | Article Recommendations | Supporting Information

ABSTRACT: Hydrogen-bonded supramolecular polymers exhibit a unique combination of structural, thermodynamic, and dynamic properties due to their reversible, noncovalent monomer associations. However, the precise mechanism underlying this process remains elusive. In this work, we focus on the supramolecular polymerization of 2,4-bis(2-ethylhexylureido)toluene (EHUT), which self-assembles into filament and tube structures in the nonpolar solvent cyclohexane via hydrogen bonding under ambient pressure and controlled temperatures. To investigate this temperature-dependent self-assembly behavior, we developed a transferable coarse-grained model that allows the study of EHUT supramolecular polymerization in cyclohexane. Here, we mimic temperature-dependent hydrogen bonding by tuning dipole parameters in the model by exploiting the fact that local dipole interactions dominate the hydrogen bonding. Molecular dynamics simulations based on this model successfully reproduce both filament and tube structures over a range of temperatures. We further investigated the kinetics and underlying mechanisms of EHUT self-assembly based on these simulations. The results reveal a stepwise and cooperative polymerization mechanism for the formation of filaments and tubes, respectively. This study offers a multiscale spatiotemporal characterization of EHUT self-assembly in cyclohexane and introduces a hydrogen-bond-driven coarse-grained modeling approach that can be extended to other temperature-dependent supramolecular systems.

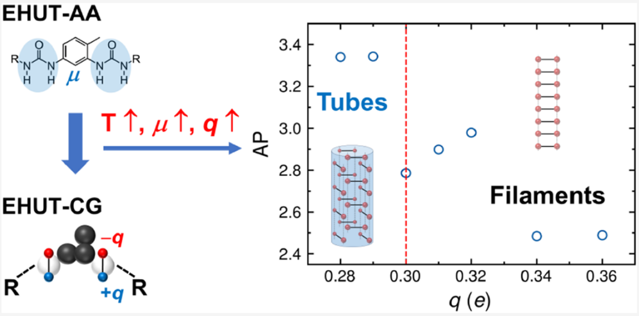

■ INTRODUCTION

Supramolecular polymers are formed through noncovalent interactions. Due to their dynamic, self-healing, adaptive, and stimulus-responsive properties,[1] supramolecular polymers have wide applications in drug delivery,[2] antimicrobial materials,[3] and reversible adhesives.[4] Common noncovalent interactions include hydrogen bonding, hydrophobic interactions, van der Waals forces, electrostatic interactions, $\pi-\pi$ stacking, metal coordination, and various combinations thereof.[1,5−10] Among them, hydrogen bonding is the core driving force for supramolecular polymer self-assembly. Its high directionality and reversibility enable precise molecular recognition and dynamic reorganization, which are essential for ordered and stimuli-responsive structures.

Experimentally, Bouteiller et al. synthesized 2,4-bis(2-ethylhexylureido)toluene (EHUT), a self-assembling molecule containing two urea groups that can form double hydrogen bonds.[11,12] These monomers can self-assemble into long-chain supramolecular polymers in nonpolar solvents. Meijer's group reported the 1,3,5-benzenetricarboxamide (BTA) supramolecular polymer formed by triple hydrogen bonds and $\pi-\pi$ stacking,[13,14] and the ureidopyrimidinone supramolecular polymer with quadruple hydrogen bonds.[15] These researches demonstrated the importance of multiple hydrogen bonds in maintaining the structural stability of the polymer. Experimental techniques such as rheology, differential scanning calorimetry, and dynamic light scattering are limited in frequency resolution, structural sensitivity, and dynamic range.[16] These limitations hinder real-time observation of the supramolecular self-assembly process at the molecular scale. However, such observation is crucial for revealing the dynamic pathways of self-assembly and identifying the underlying driving forces.

Molecular dynamics (MD) simulations provide powerful tools for analyzing self-assembly dynamics in supramolecular polymers. Common simulation methods include all-atom (AA) simulations and coarse-grained (CG) simulations.[17,18] AA simulations rely on classical force fields or first-principles data and can accurately capture atomic interactions. However, their computational cost increases significantly with system size and simulation time, making it difficult to access self-assembly dynamics on large length scales and long time scales. CG

Received: October 30, 2025
Revised: December 21, 2025
Accepted: January 21, 2026
Published: February 1, 2026

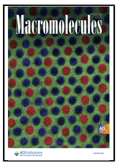

models map several atoms into a single bead, significantly reducing computational load, and are suitable for large-scale systems and long-time simulations. Common hydrogen-bonding models include the patchy particles model[19] and the charged particle model.[20] The former adds small patches to the surface of large beads to represent hydrogen-bond donors and acceptors and is suitable for simple systems. The latter introduces dipoles (positive and negative charges at a fixed distance) on the beads to simulate hydrogen bonds, taking into account both short-range and long-range interactions, making it more suitable for complex systems. In recent years, machine learning potentials (MLPs) have been widely applied in molecular simulations.[21] Researchers train models using *ab initio* molecular dynamics (AIMD) data from small systems to obtain potentials that approximate density functional theory (DFT) accuracy. These potentials are then applied to larger-scale MD simulations, achieving a balance between accuracy and efficiency. Nevertheless, the development and application of MLPs for organic systems are still in the early stages, with state-of-the-art models being optimized mostly for inorganic materials.

To study the hydrogen-bond-driven self-assembly mechanism, we chose the bisurea-based supramolecular polymer EHUT as the research system.[11,12,22] EHUT self-assembles in nonpolar solvents, which lack hydrogen-bonding capabilities. This reduces solvent−solute interactions, allowing for a more direct observation of the hydrogen-bond-driven self-assembly mechanism. EHUT monomers can self-assemble into long-chain polymers in nonpolar solvents across a range of temperatures, forming two main structures: tubes and filaments. Experimentally, it was speculated that the tube structure consists of multiple layers of cyclic molecules stacked along the tube axis, with each layer containing three EHUT molecules.[23,24] Adjacent layers are interlaced at a fixed angle. The filament structure exhibits a single-chain, fiber-like structure.[25] Experiments show that the viscosity of the tube structure is much higher than that of the filament structure.[12,22] However, existing techniques have not yet fully resolved the molecular-level assembly dynamics and microstructural evolution.

Herein, we use a charged-particle CG model based on the MARTINI force field to simulate the temperature-dependent self-assembly of EHUT, focusing on its bisurea structure. Pavan's group successfully constructed a charged-particle hydrogen-bond model in the water-soluble BTA system, revealing the cooperative mechanism from disordered aggregation to ordered stacking and fiber growth.[20,26] However, this model has a limited response to temperature changes and is not suitable for EHUT systems, where temperature plays an important role. We adjust the dipole parameters in the model to directly simulate the effect of temperature changes on the molecular interaction strength, given that hydrogen bonding is mainly driven by local dipole interactions. This approach successfully reproduces the tube-to-filament structural transition across varying temperatures, while maintaining the computational efficiency of the MARTINI CG model. Additionally, we reveal the evolution mechanism from monomer aggregation and filament extension to tube formation through a multiscale dynamic analysis. Our results could be helpful in designing tunable hydrogen-bond-driven functional materials.

■ METHODS

Development of the EHUT-CG Models

The AA molecules were modeled using the general AMBER force field (GAFF).[27] The CG molecular dynamics simulations for EHUT-CG self-assembly employ the Martini 2.2P force field.[28] We mapped each group of 2−4 heavy atoms onto a single bead according to the standard MARTINI rules. The parametrization of the EHUT-CG model was produced by the MARTINI force field. In order to better map the toluene core, we considered only the position of the methyl group. The single cyclohexane solvent was mapped to three SC1 beads. The toluene unit of EHUT was parametrized to three SC5 beads according to the aromatic ring (benzene). For the alkyl chains part, we opted to use three SC1 beads instead of two C1 beads.[20] For the urea groups part, we used a polarizable water MARTINI bead (POL),[29] containing two movable charges in order to introduce a dipole. The two charges were kept at a distance of 0.14 nm from the UR_c center, with $(-q)-UR_c-(+q)$ angle set to 180°. The value of q was optimized to reproduce the dimerization free energy profile of EHUT in cyclohexane at the atomic level.

DFT Calculations

For the isolated system, geometry optimization of EHUT was carried out using DFT with the B3LYP exchange-correlation functional[30] and the def2-TZVP basis set.[31] The GD3BJ empirical dispersion correction[32] was applied, and all calculations were performed using the Gaussian 16 C.01 package.[33] Potential energy surface scanning of EHUT was described at the B3LYP/6-31G* level[34,35] of theory. The dipole moment of EHUT was described at the B3LYP/def2-TZVPD level.[36,37] Atomic charges were calculated using the restrained electrostatic potential (RESP) method with the Multiwfn 3.8(dev) code.[38,39]

For the periodic system, geometry optimization of the preassembled tube structure was performed using the PBE-D3(BJ) exchange-correlation functional[40,41] and the DZVP-MOLOPT-SR-GTH basis set,[42] with the CP2K 2024.3 package.[43] IGMH and BCP analyses were carried out using Multiwfn, based on wavefunction data calculated with the PBE-D3(BJ)/6-311G** level.[32,44]

MD Simulations

All the simulations were carried out under the NPT ensemble (constant number of particles, pressure, and temperature) with the GROMACS 2023.3 package,[45] using the md (molecular dynamics) integrator. The temperature was kept at 25 °C for the AA simulation and at 25, 50, and 80 °C for CG simulations. The AA simulation used a 2 fs time step and CG simulation used a 20 fs time step. In all simulation, the V-rescale thermostat[46] and the Parrinello−Rahman barostat[47] were employed in the temperature and pressure baths, respectively. The temperature was maintained with a coupling constant of 1 ps in the systems. The pressure was maintained at 1 bar with a coupling constant of 5 ps in the systems. All of the simulations used isotropic pressure scaling. For electrostatic and van der Waals interactions, in all CG systems, we used a straight cutoff (1.2 nm). The particle mesh Ewald (PME)[48] approach was used to treat the long-range electrostatic effects. All the simulation maps in the article were rendered using the VMD 1.9.3 software.[49]

The dimerization free-energy profiles of the AA and CG systems were calculated using well-tempered metadynamics[50,51] simulations as implemented in the Collective Variables Module (Colvars)[52] of GROMACS. As shown in the gray beads of Figure 2a, the distance between the center of mass of the two SC5 beads located on the side chains of a single molecule and that of the remaining core bead was used as the collective variable (HILLS height = 0.1 kJ/mol; HILLS width = 0.02 nm; deposition rate = 500 time steps; bias temperature = 4000 K). The errors in the free-energy profiles of the AA and CG systems were estimated from nine free-energy profiles extracted at different times after the convergence of a single metadynamics run. The free-energy difference was defined as the difference between the minimum of the free-energy profile and the average free-energy value in the range of 1.4−1.6 nm.

https://doi.org/10.1021/acs.macromol.5c03020
Macromolecules 2026, 59, 1517−1528

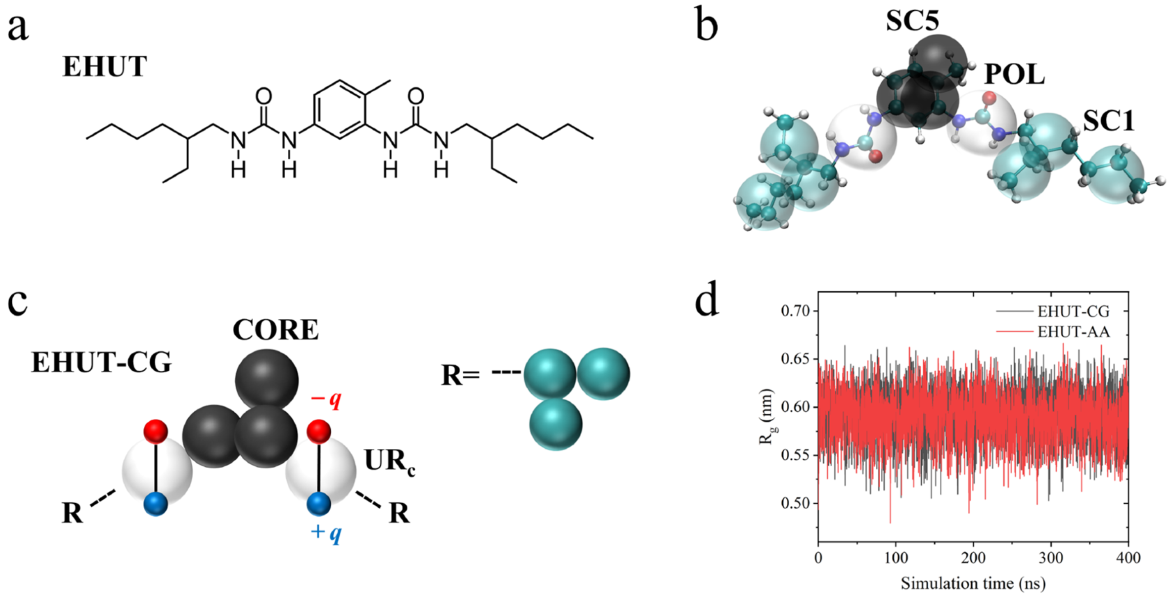

Figure 1. CG model for EHUT supramolecular polymers. (a) Chemical structure of the EHUT molecule. (b) MARTINI-based CG representation of the EHUT molecule, mapped onto 11 beads: 3 SC5 beads (toluene unit), 2 POL beads (urea groups), and 6 SC1 beads (alkyl chains). (c) CG representation of the EHUT core and the side chains. The hydrogen-bond donor and acceptor sites on the urea group are represented by a positive charge ($+q$) and a negative charge ($-q$), respectively. (d) Radius of gyration (R_g) of the EHUT molecule in both CG and AA representations, obtained from MD simulations of a single EHUT monomer in cyclohexane.

AIMD Simulations

All AIMD simulations of the preassembled tube structure were performed in the NVT ensemble using the CP2K 2024.3 package.[43] The temperature was maintained at 25 °C using the CSVR thermostat[46] with a time constant of 100 fs. The valence-shell electrons were described using the PBE exchange-correlation functional within the generalized gradient approximation (GGA).[40] Core−shell electrons were treated with Goedecker−Teter−Hutter (GTH) pseudopotentials,[53] and valence electrons were described using the hybrid Gaussian and plane-wave (GPW) method.[54] The DZVP-MOLOPT-SR-GTH basis set[42] was used, with plane-wave and relative cutoffs set to 400 and 55 Ry, respectively. Dispersion interactions were included via Grimme's correction scheme (DFT-D3).[41] Periodic boundary conditions and Γ-point sampling were applied.

Data Analysis

Amplification of Stacking Order in the EHUT Self-Assembly. For all systems, the radial distribution function $g(r)$ was calculated using the GROMACS tool *gmx rdf*.[20] The standard $g(r)$ was obtained by normalizing the number of particles in each shell to the shell volume and the average number density.

Evolution of Aggregation during EHUT Self-Assembly. We employed the *gmx clustsize* tool to monitor the self-assembly process over time, tracking the evolution of the maximum cluster size, the mean cluster size, and the total number of clusters formed in cyclohexane.[20] The average cluster size was determined by dividing the total number of monomers by the number of clusters, with a cutoff distance of 0.56 nm used to define cluster connectivity.

Average Stacking Order during EHUT Self-Assembly. The order parameter Φ, reflecting the average core−core coordination between pairs of toluene cores in EHUT, was calculated using *gmx mindist*.[20,26] A cutoff distance of 0.56 nm was applied to define ideal stacking between cores. The resulting number of contacts was normalized to the total number of monomers to yield the average coordination value.

Aggregation Propensity after the EHUT Self-Assembly Equilibrium. To evaluate the self-assembly tendency of EHUT, aggregation propensity (AP) values were calculated as the ratio of the solvent-accessible surface area (SASA) at the initial and final stages of the simulation ($\mathrm{AP} = \mathrm{SASA_{initial}}/\mathrm{SASA_{final}}$), using the default parameters of the *gmx sasa* tool (0.14 nm solvent probe).[55,56] An AP = 1 value indicates no aggregation, as $\mathrm{SASA_{final}}$ remains unchanged from the initial $\mathrm{SASA_{initial}}$. An AP > 1 value corresponds to aggregation ($\mathrm{SASA_{final}} < \mathrm{SASA_{initial}}$). Typically, aggregated systems are considered with AP ≥ 2. In this study, AP < 1 is not applicable, but it would correspond to a system undergoing disassembly ($\mathrm{SASA_{final}} > \mathrm{SASA_{initial}}$). No error is included in the AP determination, as it is based solely on the final frame of a single simulation.

■ RESULTS AND DISCUSSION

Coarse-Grained Models for EHUT

The EHUT molecule, as shown in Figure 1a, consists of a central toluene unit, middle urea groups, and terminal alkyl chains. Our primary objective was to construct a CG model that reproduces the key features of the all-atom representation, including the behavior of EHUT in the nonpolar solvent cyclohexane, the monomer−monomer interactions, and the structural differences that arise during self-assembly. To achieve this, we employed the MARTINI coarse-grained force field[57,58] owing to its demonstrated reliability in supramolecular self-assembly and its ease of implementation (Figure 1b). We further adopted the recently optimized MARTINI parameters (see **Methods**) to ensure an accurate description of molecular interactions.[20] In this model, the EHUT molecule is represented by 11 beads: 3 SC5 beads for the toluene core, 2 POL beads for the urea groups, and 6 SC1 beads for the alkyl chains.

Hydrogen bonds are directional, whereas CG models typically employ nondirectional Lennard-Jones potentials. How to represent the urea group in the CG model is the key step in our parametrization. We employ an explicit treatment of hydrogen bonding for the EHUT ureas (Figure 1c, in UR$_c$). The UR$_c$ urea beads carry a dipole represented by the ±q charges fixed at a set distance. This setting captures the rigid orientation of urea and the directional nature of hydrogen

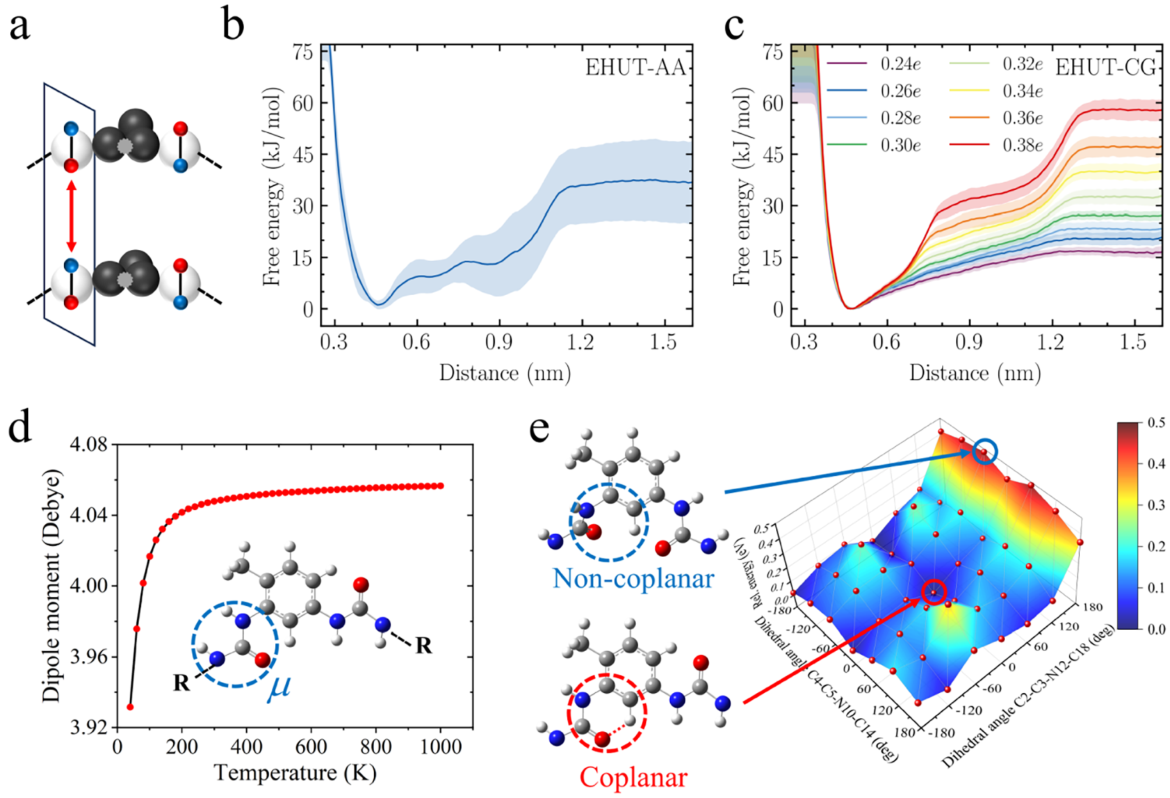

Figure 2. Schematic illustration of the directionality of the urea−urea interaction and charge fitting in the EHUT-CG model. (a) The directionality of the interaction between the UR_c beads (EHUT-CG) is explicitly imparted by the electrostatic interaction of the rigid dipoles (±q: red and blue). The gray bead represents the center of mass of the SC5 bead, which is connected to two side-chain beads. Free-energy profiles for dimerization in cyclohexane, obtained from metadynamics simulations of (b) the AA model and (c) the CG models with varying charge q (0.24e to 0.38e), under ambient conditions. (d) Temperature-dependent local dipole moment of the urea group in the EHUT molecule. (e) Flexibility potential energy surface scan of the C4−C5−N10−C14 and C2−C3−N12−C18 dihedral angles (scanned every 60°). The blue and red circles represent the noncoplanar and coplanar configurations at high and low energy states, respectively.

bonding, as observed in AA models. Following the MARTINI coarse-graining protocol, we systematically calibrate bond, angle, and dihedral parameters to replicate the conformations of atomistic monomers in cyclohexane. This parametrization strategy ensures both physical consistency with the reference system and transferability across systems. The atom-to-bead mapping of the EHUT, along with the corresponding bead order, is shown in Figure S1. The bond, angle, and dihedral distributions for both the EHUT all-atom (EHUT-AA) and coarse-grained (EHUT-CG) models are shown in Figures S2−S4. These structural parameters are in good agreement between the EHUT-CG and EHUT-AA models. At the single monomer level, the radius of gyration (R_g) of the EHUT-CG model closely matches that of the EHUT-AA model in explicit cyclohexane (Figure 1d: R_g = 0.591 ± 0.025 nm for EHUT-AA and R_g = 0.593 ± 0.025 nm for EHUT-CG). This indicates that the EHUT-CG model effectively captures the behavior of the EHUT monomer in cyclohexane while requiring significantly less computational time for the same system.

To determine the dipole parameter, we first evaluated the accuracy of the CG model in describing the interactions between monomers in solution. The schematic representation of the EHUT pair is shown in Figure 2a, where blue beads (+q) and red beads (−q) indicate hydrogen-bond donors and acceptors, respectively. The variable of the free energy corresponds to the distance between the dimers, defined as the centroid distance of the two SC5 beads attached to the side chains (the gray beads in Figure 2a). Using metadynamics,[50,51,59] we obtained the free energy of dimerization for both the EHUT-AA and EHUT-CG models under ambient conditions (Figure 2b,c). For the EHUT-CG model, we calculated a series of free energy profiles at various charge q, aiming to determine the q range that best matches the EHUT-AA reference. The free energy curves of both the EHUT-AA and EHUT-CG models have their minima at approximately 0.47 nm, with a plateau starting at around 1.3 nm. The difference between the minimum point and the plateau represents the free energy of association. The free energy range for the EHUT-AA model is between 25.25 and 48.99 kJ/mol (Figure 2b). We found that the free energy curves of the EHUT-CG model at different charge values (0.28e to 0.36e) fall within the free energy range of the EHUT-AA model (Figure 2c).

To elucidate the origin of the multiple charge parameter q, we use DFT calculations to investigate how the dipole moment of a single EHUT molecule varies with temperature. First, the conformational search of the EHUT molecule was performed using Grimme's xtb program (GFN-xTB method)[60,61] to obtain the ten lowest-energy structures. The local dipole moment of the urea group varied for each conformation. Second, we calculate the dipole moment of the urea group at different temperatures using the Molclus program.[62] For each temperature, we first obtain the relative free energy of ten representative conformations. The overall dipole moment at

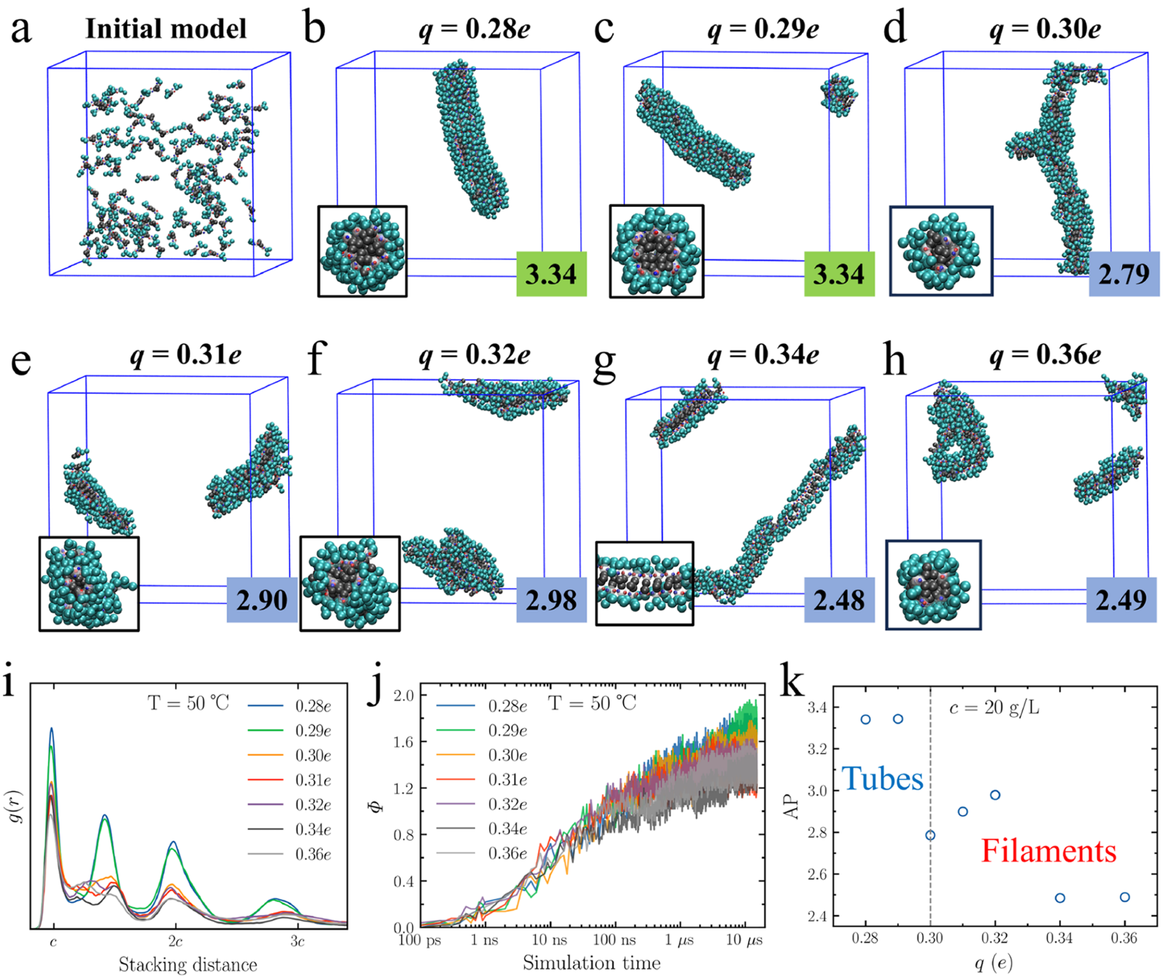

Figure 3. EHUT self-assembly simulations at 20 g/L under varying charge values q. (a) The initial model consisting of 100 EHUT molecules in cyclohexane (for clarity, only the EHUT monomers are shown). Final structures after 15 μs are for (b) $q = 0.28e$ (tube), (c) $q = 0.29e$ (tube), (d) $q = 0.30e$ (filament), (e) $q = 0.31e$ (filament), (f) $q = 0.32e$ (filament), (g) $q = 0.34e$ (filament), and (h) $q = 0.36e$ (filament). Results are colored according to the structures formed: filaments (blue) and tubes (green). Structures show the cross-section in the inset. (i) Radial distribution functions $g(r)$ of EHUT cores for different q values at 50 °C. (j) Order parameter Φ (core−core coordination) as a function of time in EHUT-CG simulations at 50 °C. (k) AP scores as a function of charge q, illustrating the structural behavior of the EHUT self-assembly.

each temperature is then computed as a weighted average of the dipole moments of these ten conformations, with the weights determined by their Boltzmann-derived populations. Finally, the local dipole moment μ of the urea group (indicated by the blue dashed circle) increases with temperature, as shown in Figure 2d. These temperature-induced changes in dipole moment are not accounted for in all-atom classical MD simulations, where atomic charges are predefined by the force field and remain fixed regardless of temperature. As a result, such simulations may fail to capture the temperature dependence of hydrogen bonding, as they cannot reflect the subtle variations in electrostatic interactions driven by thermal fluctuations.

We further perform a flexibility potential energy surface scan for the EHUT monomer, which offers support for the above proposition. The dihedral angles C4−C5−N10−C14 and C2−C3−N12−C18 are scanned at 60° intervals using DFT calculations (see Figure 2e and Figure S5). We find that low-energy conformations exhibit a planar alignment between the urea groups and the molecular core, corresponding to smaller dipole moments (lower q values). In contrast, higher-energy conformations show a nonplanar arrangement, associated with larger dipole moments (higher q values). When the urea group is coplanar with the core, it facilitates the formation of weak C−H···O hydrogen bonds, leading to a slight reduction in the dipole moment of the urea group. Conversely, the absence of this interaction in nonplanar conformations leads to a larger dipole moment. These results suggest that temperature variations can alter the local charge distribution, which, in turn, affects the relative orientation between the urea group and the molecular core. This mechanism may underlie the temperature-dependent structural behavior observed in experiments.[16,22]

Dynamic Behavior at Different q Values

In our coarse-grained model, we represent an increase in temperature by increasing the charge parameter q, based on the DFT-calculated trend shown in Figure 2d. After validating the EHUT-CG parameters, we perform MD simulations on the EHUT-CG model with varying charge q, while keeping the bond parameters fixed. However, the number of monomers that can be realistically simulated in explicit-solvent systems is limited by the high computational cost associated with solvent particles and long simulation times. As a result, the simulated system is overconcentrated (in our case, ∼1−2 orders of magnitude higher than experiments).[22] While decreasing the concentration by reducing the number of monomers or enlarging the simulation box is possible, it often leads to poor statistical significance or impractically high computational cost. Thus, we select a concentration of 20 g/L (100 EHUT monomers dispersed in 20000 cyclohexane molecules) for the simulations. The simulated concentration is five times higher than the concentration in Burger's experiments (4 g/L).[22] The initial model consisting of 100 EHUT molecules in cyclohexane is shown in Figure 3a. The snapshots of the EHUT-CG simulations (15 μs) after equilibration with different charge values (q) are shown in Figure 3b−h. For the sake of clarity, only the EHUT monomers are displayed in all simulation figures. The self-assembled structure of EHUT-CG forms a thick filament, defined as a tube composed of four filaments (Figure 5a,c), when $q = 0.28e$ and $q = 0.29e$. In our simulations, no solvent molecules are present within the cavity of the tube assemblies. As q increases from 0.30e, the structure transitions into a thin filament, defined in this study as a structure composed of one to two filaments (Figure 5a,b), and this morphology remains consistent for q values ranging from 0.31e to 0.36e. The difference in the self-assembled structure at different values of q suggests that the slight variations in the dipole moment induced by temperature significantly influence the self-assembly behavior of EHUT.

The radial distribution function $g(r)$ describes the relative probability of locating neighboring EHUT cores at defined stacking distances (c for the closest neighbor, 2c for the second neighbor, and 3c for the third neighbor). We computed $g(r)$ for EHUT cores based on the equilibrated trajectories (final 2 μs of each simulation), which serve as reliable indicators of stacking order. Because the data are averaged over all monomers, the relative intensities of the $g(r)$ peaks at c, 2c, and 3c reflect the degree of structural organization within the assemblies. In general, higher $g(r)$ peaks at these stacking intervals correspond to better ordering and enhanced stability of core stacking.

As shown in Figure 3i, the peaks in $g(r)$ at stacking distances c, 2c, and 3c become increasingly sharp as the charge parameter q decreases. This trend indicates enhanced stacking order and stronger intermolecular interactions within the assemblies. In addition to these main peaks, a distinct secondary peak emerges between c and 2c, corresponding to the distance between EHUT monomers in adjacent filaments (see Figure S6a). This interfilament peak is notably more intense at q = 0.28−0.29e than at q = 0.30−0.36e, suggesting tighter packing between filaments at lower q. These findings reveal that EHUT self-assembles into tube structures at lower q values (i.e., lower temperatures) and into individual filaments at higher q values (i.e., higher temperatures), in agreement with experimental observations.[22] Figure 3b−h further supports this interpretation by directly visualizing tube formation under low-q conditions.

The molecular systems consisting of 100 EHUT-CG monomers, initially dispersed in cyclohexane, provide an insightful case study of the dynamics (Figure 3a). During the early stages of coarse-grained molecular dynamics (CG-MD) simulations (∼0 to 100 ns), monomers rapidly aggregate, as evidenced by the sharp decline in the number of EHUT clusters in solution (Figure S11b). The Φ index, representing the average coordination number between EHUT cores (see Figure S6b), ranges from 0 (fully dispersed) to a theoretical maximum of 2 (perfect stacking with two neighboring monomers). The time evolution of the order parameter Φ (core−core coordination) indicates that EHUT assemblies remain largely disordered during the first ∼1 μs (Figure 3j). As the simulation progresses, the Φ index increases significantly, reaching approximately 1.8 after 15 μs for $q = 0.28e$ and $q = 0.29e$. For $q = 0.36e$, the Φ index stabilizes at a lower value of ∼1.4. Notably, during the CG-MD simulation, the largest EHUT assembly spontaneously evolved into a 100-mer cluster, as illustrated in Figure S9b and Figure S10b. Interestingly, a lower charge q is associated with a higher Φ value, indicating an enhanced stacking order. These findings align with previous $g(r)$ analysis, reinforcing that while initial aggregation occurs rapidly, the establishment and amplification of stacking order within the oligomers proceed at a much slower pace.

In order to better evaluate the self-assembly tendency, we calculated the AP of the EHUT systems at different q values. AP values were calculated as the ratio of the SASA at the initial and final stages of the simulation.[55,56] The AP values are shown in the bottom right corner of Figure 3b−h. For all simulations with different q values, the AP value remained above 2, indicating a strong aggregation tendency across all systems. Experimental observations further confirm that EHUT molecules exhibit a high propensity for self-assembly via hydrogen bonding, forming stable aggregates consistent with our simulation-derived AP values.[22] The AP values depend on q values, as shown in Figure 3k; at lower q values, AP exceeds 3, indicating stronger self-assembly. Notably, the tube structure exhibits AP values above 3, whereas the filament structure remains below this threshold. The AP values exhibit a slightly nonmonotonic behavior at $q = 0.31e$ and $q = 0.32e$, where the structures consist mainly of multiple short filaments due to the relatively high q. In contrast, long filaments are observed at $q = 0.34e$ and $q = 0.36e$. In both cases, the AP values of the short- and long-filament structures remain below 3. This suggests that lower q values promote tube formation with stronger aggregation, whereas higher q values favor filament structures with weaker aggregation.

Recently, temperature-dependent experiments have shown that, at a concentration of 4 g/L, EHUT tubes are formed in cyclohexane below 49 °C.[22] When the temperature exceeds this threshold, the tubes undergo a transition into filament structures. In the EHUT system, higher concentrations lead to higher transition temperatures. Given that our system has a concentration of 20 g/L, the transition temperature is expected to exceed 49 °C but remain below 80°C, considering the boiling point of cyclohexane. Therefore, we evaluated the system's behavior at different temperatures (25 °C, 50 °C, and 80 °C), taking into account the accuracy of our model.

To test the temperature sensitivity of our CG models, we performed a quantitative analysis from three aspects: (i) radial distribution function $g(r)$, (ii) order parameter Φ, and (iii) cluster analysis (see **Methods** for details). First, (i) at 25 °C, the peaks at c, 2c, and 3c are lower than those observed at 50 °C and 80 °C, although the overall trend remains consistent: lower q values result in higher peak intensities at all positions. The relatively weaker peaks at 25 °C are attributed to the limited simulation time (15 μs), which may be insufficient for full equilibration at lower temperatures. Extending the simulation to 25 °C would incur significantly higher computational costs. Notably, the weak temperature sensitivity of our CG model is consistent with previous reports, suggesting that the model reliably captures room-temperature behavior. At higher temperatures, shorter simulations suffice to reach

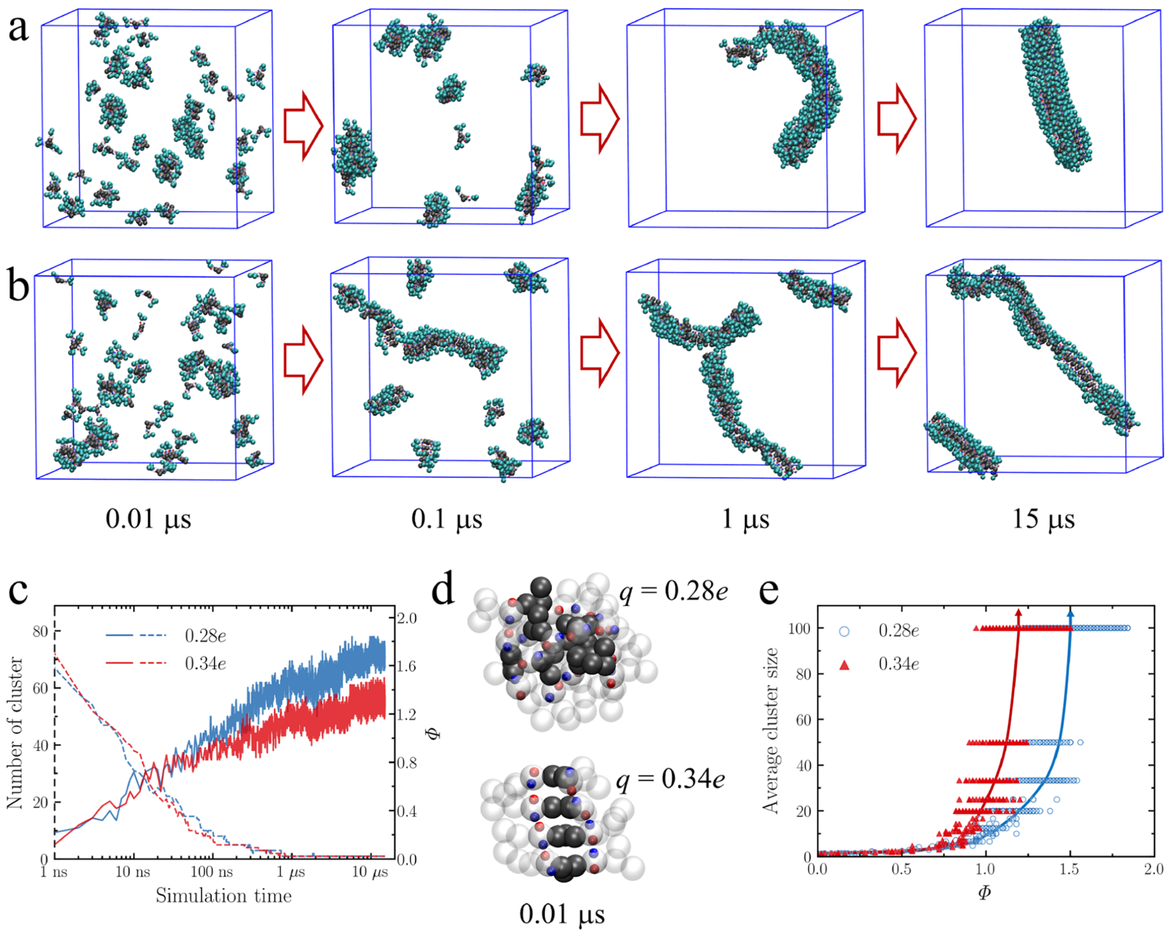

Figure 4. Self-assembly of EHUT molecules into tube and filament structures. Snapshots at 0.01 μs, 0.1 μs, 1 μs, and 15 μs for the 100 EHUT-CG self-assembly system at charges (a) $q = 0.28e$ and (b) $q = 0.34e$. (c) Number of EHUT clusters and order parameter Φ (core−core coordination) as a function of CG-MD simulation time for the 100 EHUT self-assembling systems at both $q = 0.28e$ (blue) and $q = 0.34e$ (red). (d) Snapshots with local magnification at 0.01 μs for the 100 EHUT-CG self-assembly system at $q = 0.28e$ (top) and $q = 0.34e$ (bottom). For clarity, all SC1 beads were rendered as ghost atoms. (e) CG-MD trajectories as a function of average cluster size and Φ.

structural equilibrium due to the time−temperature effect. Second, (ii) the Φ index shows a similar temperature dependence, increasing with temperature (Figure 3j and Figure S8). At 25 °C, Φ remains relatively low throughout the 15 μs simulation, suggesting incomplete structural evolution. In contrast, at 50 and 80 °C, Φ stabilizes at higher values, indicating that elevated temperature accelerates equilibration. These results align with the trends observed in $g(r)$ and reinforce the time−temperature effect. Finally, (iii), as shown in Figures S9−S11, cluster analysis of EHUT at the three temperatures reveals consistent behavior. In all cases, EHUT monomers initially aggregate slowly over the first ∼0−100 ns. The average and maximum cluster sizes reach their peak values (approximately 100 monomers) around ∼1 μs, regardless of the temperature or charge q. Between 1 and 15 μs, the cluster sizes remain stable. Simultaneously, the number of clusters rapidly decreases to a minimum (∼1−2) within the first ∼1 μs and remains low thereafter. These findings indicate that the temperature mainly accelerates the dynamics of self-assembly but does not alter the underlying kinetic trends. Considering the time−temperature effect and computational cost, we focus our subsequent discussion on the mechanism and dynamics of EHUT supramolecular polymerization at 50 °C.

Mechanism of EHUT Self-Assembly in Cyclohexane

In order to more accurately describe the dynamic behavior of the 100 EHUT-CG self-assembly system at different charge values (q), we plotted the CG-MD trajectories at different simulation times (0.01, 0.1, 1, and 15 μs). We selected $q = 0.28e$ (tube, Figure 4a) and $q = 0.34e$ (filament, Figure 4b) as representative cases for analyzing the self-assembly process. At the early stage (0.01 μs), EHUT-CG monomers with $q = 0.28e$ and $q = 0.34e$ aggregate, initially forming multiple small clusters. By 0.1 μs, the number of clusters decreased significantly in both cases. However, at $q = 0.28e$, tube structures have not yet formed, while at $q = 0.34e$, filament structures begin to emerge. Notably, by 1 μs, distinct tube and filament structures are observed for $q = 0.28e$ and $q = 0.34e$, respectively. At this stage, both systems exhibit a single large cluster (Figure 4c, in dashed lines), with the tube structure remaining flexible. The Φ index (Figure 4c, in solid lines) indicates an ordered state in both cases, with a higher average Φ value for $q = 0.28e$ compared to $q = 0.34e$. At the final equilibrium state (15 μs), the tube structure becomes more rigid, while the filament straightens.

These morphological differences suggest distinct assembly mechanisms. To investigate this, we analyzed the early-stage self-assembly behavior by magnifying a snapshot at 0.01 μs (Figure 4d). In the tube-forming system ($q = 0.28e$), EHUT

https://doi.org/10.1021/acs.macromol.5c03020
Macromolecules 2026, 59, 1517−1528

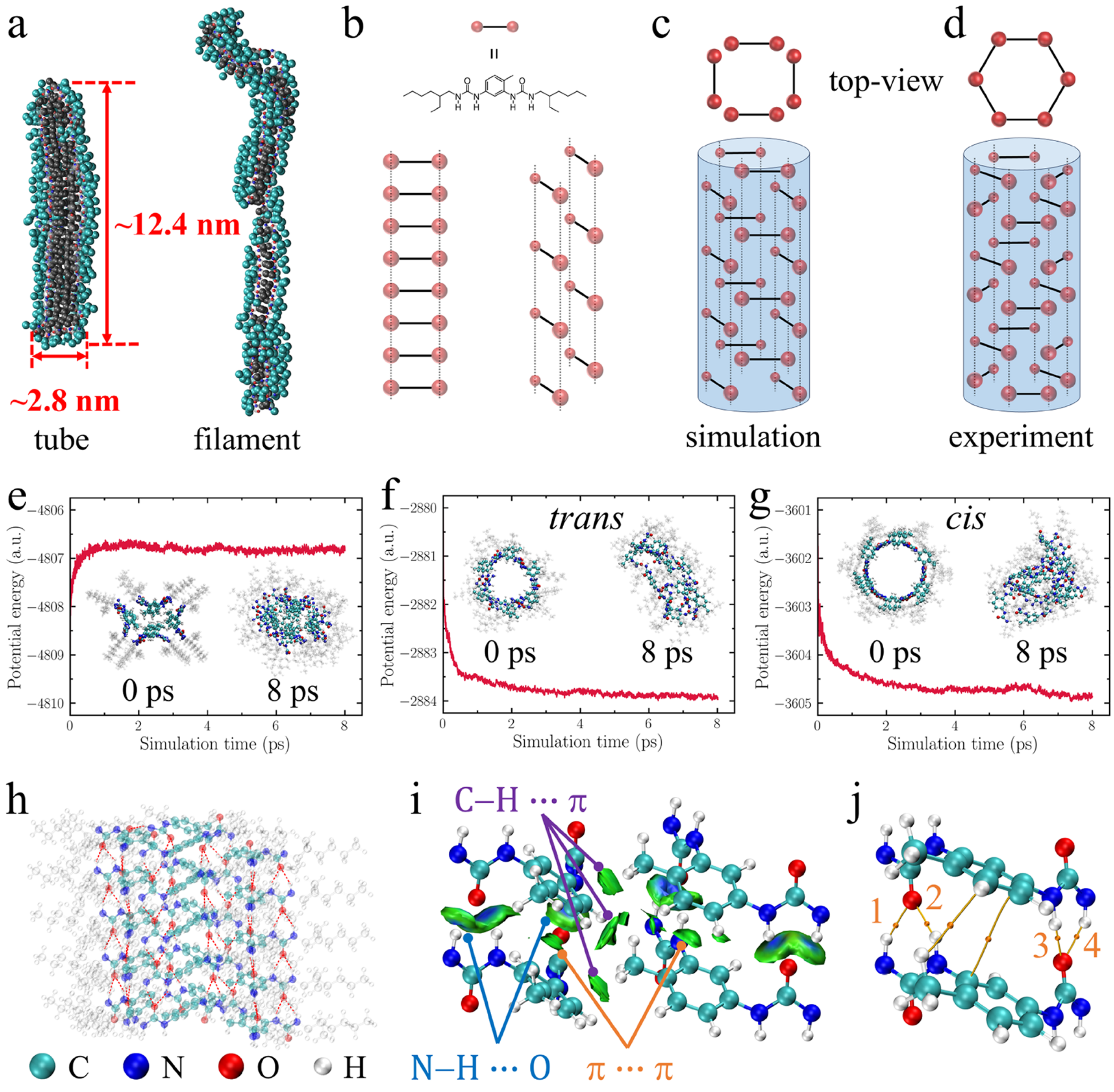

Figure 5. Mechanism of EHUT self-assembly in cyclohexane. (a) Tube and filament structures formed by EHUT self-assembly (cross-sectional view for the tube). (b) Schematic representation of two filament types: monomolecular and bimolecular. EHUT molecules are depicted as dumbbells with red spheres representing urea groups. Hydrogen bonds are shown as dashed lines connecting the urea groups. (c) Schematic of the EHUT tube obtained from simulations, with the top view shown above. (d) Proposed tube structure based on experimental hypotheses with the corresponding top view above. Potential energy evolution of preassembled EHUT structures in AIMD simulations: (e) simulation-derived structure; (f) experimentally proposed *trans* structure; (g) experimentally proposed *cis* structure. Snapshots at 0 and 8 ps are shown. (h) DFT calculations of all-atom EHUT molecules preassembled into the tube structure based on CG simulations. The red dashed lines indicate hydrogen bonds. (i) IGMH interaction analysis of EHUT fragments (isosurface: 0.003 au). (j) BCP (brown dots) analysis between two EHUT fragments (alkyl chains excluded for clarity). Numbers 1, 2, 3, and 4 indicate the BCP of the four hydrogen bonds. Figure 5i,j shows fragment structures derived from Figure 5h (for clarity, only the preassembled portion of the EHUT molecules is shown).

monomers aggregate into disordered clusters. In contrast, at $q = 0.34e$, monomers bypass large disordered clusters and directly assemble into short ordered filaments. We further analyzed the evolution of the system in terms of the average cluster size and the order parameter Φ (Figure 4e). At both $q = 0.28e$ and $q = 0.34e$, EHUT monomers initially assemble into disordered clusters comprising approximately 2−10 molecules (Φ in the range of 0−0.8). These small clusters gradually merge into larger ones comprising approximately 50−100 molecules (Φ in the range of 1.2−2.0). As the system evolves, the arrangement becomes increasingly ordered, leading to well-defined supramolecular assemblies, as reflected in the discrete steps in the top-right region of the plot.

The interplay between directional hydrogen bonding and nondirectional electrostatic interactions governs the self-assembly pathways and the resulting morphologies. For filament structures, a larger hydrogen bond dipole moment (q value) enhances electrostatic interactions, promoting the formation of ordered, small clusters from the beginning. These clusters then grow by stepwise polymerization, where monomers or small clusters sequentially merge with existing ordered structures, promoting one-dimensional growth of the filaments. In contrast, tube structures follow cooperative polymerization. The system first forms a large disordered aggregate, which then undergoes continuous molecular rearrangement and optimization of the hydrogen bond network. This process gradually increases the order of the structure, leading to the formation of a tubular structure.

Further, we perform a quantitative analysis of the tube and filament structures. The tube has a diameter of ~2.8 nm and a length of ~12.4 nm (Figure 5a, in the tube). In contrast, the filament is thinner and longer compared to the tube (Figure 5a, in the filament). The schematic diagram of the filament self-assembly equilibrium state is shown in Figure 5b, where the filament consists of one or two thin filaments. This structural feature is consistent with the 15 μs simulation snapshot presented in Figure 4b. Moreover, the calculated linear density of the simulated preassembled filament is consistent with the experimental values, as shown in Table 1 and Figure S13a.

Table 1. Linear Density of EHUT Self-Assemblies in Experiment (n_{exp}) and *Ab Initio* Molecular Dynamics Simulation (n_{AIMD})

Structure	n_{exp} (Å^{-1})	n_{AIMD} (Å^{-1})
Filament	0.23[a]	0.20
Tube	0.57[b]	0.65

[a] The filament structure is characterized by a linear density of 0.2−0.3. The values were obtained in $CDCl_3$ at 32 mM. [b] The tube structure is characterized by a linear density of 0.5−0.7. The values were obtained in D_8-toluene at 12 mM.[24]

These results demonstrate that the filament structure obtained from simulation is in good agreement with the experimental observations. Similarly, after 15 μs of equilibration, the tube structure is shown in Figure 4a. Our simulations reveal that the tube structure consists of four filaments assembled side-by-side, with EHUT monomers adopting a staggered arrangement between adjacent filaments (Figure 5c). However, experimental studies propose an alternative model, where the tube acts as a modular building block that stacks in a brick-like fashion (Figure 5d). This comparison highlights distinct differences between the simulated and experimental tube structures in terms of the molecular packing and hierarchical assembly.

To evaluate the consistency between the simulation results and the experimental hypothesis, we performed AIMD simulations on both the simulated and experimentally proposed preassembled tubes.[23] The plots of potential energy versus simulation time for the simulated and experimental preassembled tubes are shown in Figure 5e−g. As shown in Figure 5e, the simulated tube structure, initially preassembled at the beginning, retains its tubular morphology after reaching equilibrium at 8 ps, as indicated by the plateau in potential energy. In contrast, the experimental preassembled tube, starting as a tube at 0 ps, collapses by 8 ps. Both the *trans* and *cis* preassembled structures fail to retain their structural integrity, as shown in Figure 5f,g, with their respective configurations depicted in Figure S12. Furthermore, the linear density of the simulated preassembled tube obtained from AIMD calculations is consistent with the experimental values, falling within the range characteristic of the tubular structure, as shown in Table 1 and Figure S13b. These results demonstrate that the simulated tube structure better reflects both the thermodynamic stability and the kinetic resilience of the system.

Additionally, we performed DFT geometry optimizations on the simulated preassembled tube structures. Figure 5h shows the optimized configurations, which remain stable and preserve the characteristic tubular morphology. Importantly, a large number of hydrogen bonds are retained in the optimized structure (Figure 5h, shown in red dashed lines), highlighting hydrogen bonding as a key factor in stabilizing the tube. In contrast, the experimentally proposed preassembled AIMD tube structure collapses due to an insufficient number of hydrogen bonds. These findings support the conclusion that hydrogen-bond-driven self-assembly is better captured by the simulated structure.

We further explored the mechanism underlying tube formation in simulations by examining the interactions between EHUT molecular fragments via DFT calculations, using the independent gradient model based on Hirshfeld partitioning (IGMH).[63] Figure 5i illustrates the interactions in the simulated tube. The results show that tube formation mainly relies on N−H···O, C−H···π, and π−π interactions. Further analysis reveals that a single filament is mainly held together by strong N−H···O hydrogen bonds (blue areas and large electron clouds indicate strong interactions) and weaker π−π interactions (smaller electron clouds). In contrast, the tube formed by four filaments relies mainly on weak C−H···π interactions. Although individual C−H···π interactions are weak, their cumulative effect among multiple filaments results in a stable structure.

Finally, we analyzed the BCP between two EHUT molecules to determine whether the interactions are bonding or nonbonding (Figure 5j). The yellow spheres in the figure represent BCPs, and the values for each point are given in Table 2. The analysis shows that the Laplacian of electron density and binding energy are both positive, indicating that all interactions are nonbonding. The table also lists four hydrogen bonds at different positions, and their interaction energies are similar, suggesting that the hydrogen bond strengths are approximately equal. We substituted the electron density values at the BCPs of the four hydrogen bonds into the empirical hydrogen bond energy estimation formula developed by Lu et al.: $\Delta E \approx -223.08 \times \rho_{\text{BCP}} + 0.7423$.[64] The resulting hydrogen bond energies, summarized in Table 2, range from −5.0 to −5.9 kcal/mol. Although a single hydrogen bond is relatively weak, a urea group can form strong double hydrogen bonds (−11 kcal/mol), and one EHUT molecule can form up to eight hydrogen bonds. These results explain why even experimentally small amounts of EHUT can readily form a high-viscosity tubular system under ambient conditions.

Table 2. Bond Critical Point (BCP) Properties: Electron Density (ρ_{BCP}), Laplacian of Electron Density ($\nabla^2 \rho_{\text{BCP}}$), and Binding Energy ($\Delta E$)

Bond	ρ_{BCP} (a.u.)	$\nabla^2 \rho_{\text{BCP}}$ (a.u.)	ΔE (kcal/mol)
N−H_1···O[a]	0.0299	0.1097	−5.9
N−H_2···O[a]	0.0278	0.1043	−5.5
N−H_3···O[a]	0.0299	0.1089	−5.9
N−H_4···O[a]	0.0258	0.0961	−5.0
C−H···π	0.0032	0.0099	-
π···π	0.0032	0.0079	-

[a] The values labeled 1, 2, 3, and 4 of N−H···O in the table correspond to the four hydrogen bonds shown in Figure 5j.

■ CONCLUSIONS

In this work, we have developed a portable, temperature-dependent coarse-grained model based on the MARTINI force field. The model investigates the supramolecular polymerization and dynamic self-assembly of EHUT in the nonpolar solvent cyclohexane. Simulations based on this model successfully reproduce both filament and tube structures observed in experiments at various temperatures. We performed AIMD calculations on both the simulated and experimentally hypothesized preassembled tube structures. The results show that the simulated tube, formed by the staggered association of four filaments, is more thermodynamically and kinetically stable. The simulated filament structure agrees well with the experimental observations.

Molecular dynamics simulations reveal that lower dipole values weaken intermolecular interactions, favoring the formation of tube structures. At higher dipole values, the system prefers the growth of elongated filament structures. The formation mechanisms are distinct: filaments form via stepwise polymerization, while tubes assemble through cooperative polymerization. We further analyzed the intermolecular interactions within the preassembled structures using DFT calculations. Filament formation is mainly driven by hydrogen bonding, whereas tube formation involves not only hydrogen bonding but also C−H···π and π···π interactions. This model provides new insights into the temperature-dependent dynamics and mechanisms of hydrogen-bonded supramolecular polymers. These findings provide theoretical guidance for the design of controllable supramolecular polymers.

■ ASSOCIATED CONTENT

Supporting Information

The Supporting Information is available free of charge at https://pubs.acs.org/doi/10.1021/acs.macromol.5c03020.

All-atom force field files for EHUT in cyclohexane, including topology (.itp) and coordinate (.pdb) files for both EHUT and cyclohexane (ZIP)

Supplemental figures (PDF)

■ AUTHOR INFORMATION

Corresponding Author

Jiajia Zhou − *South China Advanced Institute for Soft Matter Science and Technology, School of Emergent Soft Matter, South China University of Technology, Guangzhou 510640, China; Guangdong Provincial Key Laboratory of Functional and Intelligent Hybrid Materials and Devices, South China University of Technology, Guangzhou 510640, China;* orcid.org/0000-0002-2258-6757; Email: zhouj2@scut.edu.cn

Authors

Nengjie Cao − *South China Advanced Institute for Soft Matter Science and Technology, School of Emergent Soft Matter, South China University of Technology, Guangzhou 510640, China*

Fengxiang Zhou − *South China Advanced Institute for Soft Matter Science and Technology, School of Emergent Soft Matter, South China University of Technology, Guangzhou 510640, China*

Xianggui Zhou − *South China Advanced Institute for Soft Matter Science and Technology, School of Emergent Soft Matter, South China University of Technology, Guangzhou 510640, China*

Jinyuan Mao − *South China Advanced Institute for Soft Matter Science and Technology, School of Emergent Soft Matter, South China University of Technology, Guangzhou 510640, China;* orcid.org/0000-0003-2496-777X

Xiangmeng Jia − *South China Advanced Institute for Soft Matter Science and Technology, School of Emergent Soft Matter, South China University of Technology, Guangzhou 510640, China;* orcid.org/0000-0002-4056-747X

Complete contact information is available at: https://pubs.acs.org/10.1021/acs.macromol.5c03020

Notes

The authors declare no competing financial interest.

■ ACKNOWLEDGMENTS

This research was supported by the Advanced Materials-National Science and Technology Major Project (2025ZD0614503), the National Natural Science Foundation of China (Grant No. 22373036), and the R&D Program of Guangzhou (Grant No. 2024D03J0007). The computation of this work was made possible by the facilities of Information and Network Engineering and Research Center of SCUT.

■ REFERENCES

(1) Aida, T.; Meijer, E.; Stupp, S. Functional supramolecular polymers. *Science* **2012**, *335*, 813−817.

(2) Le, Z.; Chen, Y.; Han, H.; Tian, H.; Zhao, P.; Yang, C.; He, Z.; Liu, L.; Leong, K. W.; Mao, H.-Q.; Liu, Z.; Chen, Y. Hydrogen-bonded tannic acid-based anticancer nanoparticle for enhancement of oral chemotherapy. *ACS Appl. Mater. Interfaces* **2018**, *10*, 42186−42197.

(3) Chen, C.; Pan, F.; Zhang, S.; Hu, J.; Cao, M.; Wang, J.; Xu, H.; Zhao, X.; Lu, J. R. Antibacterial activities of short designer peptides: a link between propensity for nanostructuring and capacity for membrane destabilization. *Biomacromolecules* **2010**, *11*, 402−411.

(4) Zhang, Q.; Li, T.; Duan, A.; Dong, S.; Zhao, W.; Stang, P. J. Formation of a supramolecular polymeric adhesive via water−participant hydrogen bond formation. *J. Am. Chem. Soc.* **2019**, *141*, 8058−8063.

(5) Da Silva, R. M.; Van Der Zwaag, D.; Albertazzi, L.; Lee, S. S.; Meijer, E. W.; Stupp, S. I. Super-resolution microscopy reveals structural diversity in molecular exchange among peptide amphiphile nanofibres. *Nat. Commun.* **2016**, *7* (1), 11561.

(6) Brunsveld, L.; Folmer, B. J.; Meijer, E. W.; Sijbesma, R. P. Supramolecular polymers. *Chem. Rev.* **2001**, *101*, 4071−4098.

(7) Krieg, E.; Bastings, M. M.; Besenius, P.; Rybtchinski, B. Supramolecular polymers in aqueous media. *Chem. Rev.* **2016**, *116*, 2414−2477.

(8) Yang, L.; Tan, X.; Wang, Z.; Zhang, X. Supramolecular polymers: historical development, preparation, characterization, and functions. *Chem. Rev.* **2015**, *115*, 7196−7239.

(9) Cantekin, S.; de Greef, T. F.; Palmans, A. R. Benzene-1, 3, 5-tricarboxamide: a versatile ordering moiety for supramolecular chemistry. *Chem. Soc. Rev.* **2012**, *41*, 6125−6137.

(10) Garzoni, M.; Cheval, N.; Fahmi, A.; Danani, A.; Pavan, G. M. Ion-selective controlled assembly of dendrimer-based functional nanofibers and their ionic-competitive disassembly. *J. Am. Chem. Soc.* **2012**, *134*, 3349−3357.

(11) Lortie, F.; Boileau, S.; Bouteiller, L.; Chassenieux, C.; Demé, B.; Ducouret, G.; Jalabert, M.; Lauprêtre, F.; Terech, P. Structural and rheological study of a bis-urea based reversible polymer in an apolar solvent. *Langmuir* **2002**, *18*, 7218−7222.

(12) Bouteiller, L.; Colombani, O.; Lortie, F.; Terech, P. Thickness transition of a rigid supramolecular polymer. *J. Am. Chem. Soc.* **2005**, *127*, 8893−8898.

(13) Baker, M. B.; Albertazzi, L.; Voets, I. K.; Leenders, C. M.; Palmans, A. R.; Pavan, G. M.; Meijer, E. Consequences of chirality on

the dynamics of a water-soluble supramolecular polymer. *Nat. Commun.* **2015**, *6*, 6234.

(14) Garzoni, M.; Baker, M. B.; Leenders, C. M.; Voets, I. K.; Albertazzi, L.; Palmans, A. R.; Meijer, E.; Pavan, G. M. Effect of H-bonding on order amplification in the growth of a supramolecular polymer in water. *J. Am. Chem. Soc.* **2016**, *138*, 13985−13995.

(15) Sijbesma, R. P.; Beijer, F. H.; Brunsveld, L.; Folmer, B. J.; Hirschberg, J. K.; Lange, R. F.; Lowe, J. K.; Meijer, E. Reversible polymers formed from self-complementary monomers using quadruple hydrogen bonding. *Science* **1997**, *278*, 1601−1604.

(16) Burger, N. A.; Pembouong, G.; Bouteiller, L.; Vlassopoulos, D.; Loppinet, B. Complete dynamic phase diagram of a supramolecular polymer. *Macromolecules* **2022**, *55*, 2609−2614.

(17) Bochicchio, D.; Pavan, G. M. Molecular modelling of supramolecular polymers. *Adv. Phys.:X* **2018**, *3*, 1436408.

(18) Jayaraman, A. 100th anniversary of macromolecular science viewpoint: modeling and simulation of macromolecules with hydrogen bonds: challenges, successes, and opportunities. *ACS Macro Lett.* **2020**, *9*, 656−665.

(19) Kulshreshtha, A.; Hayward, R. C.; Jayaraman, A. Impact of composition and placement of hydrogen-bonding groups along polymer chains on blend phase behavior: coarse-grained molecular dynamics simulation study. *Macromolecules* **2022**, *55*, 2675−2690.

(20) Bochicchio, D.; Pavan, G. M. From cooperative self-assembly to water-soluble supramolecular polymers using coarse-grained simulations. *ACS Nano* **2017**, *11*, 1000−1011.

(21) Zhang, L.; Han, J.; Wang, H.; Car, R.; Weinan, E. Deep potential molecular dynamics: a scalable model with the accuracy of quantum mechanics. *Phys. Rev. Lett.* **2018**, *120* (14), 143001.

(22) Burger, N. A.; Mavromanolakis, A.; Meier, G.; Brocorens, P.; Lazzaroni, R.; Bouteiller, L.; Loppinet, B.; Vlassopoulos, D. Stabilization of supramolecular polymer phase at high pressures. *ACS Macro Lett.* **2021**, *10*, 321−326.

(23) Shikata, T.; Nishida, T.; Isare, B.; Linares, M.; Lazzaroni, R.; Bouteiller, L. Structure and dynamics of a bisurea-based supramolecular polymer in n-dodecane. *J. Phys. Chem. B* **2008**, *112*, 8459−8465.

(24) Isare, B.; Linares, M.; Lazzaroni, R.; Bouteiller, L. Engineering the cavity of self-assembled dynamic nanotubes. *J. Phys. Chem. B* **2009**, *113*, 3360−3364.

(25) Brocorens, P.; Linares, M.; Guyard-Duhayon, C.; Guillot, R.; Andrioletti, B.; Suhr, D.; Isare, B.; Lazzaroni, R.; Bouteiller, L. Conformational plasticity of hydrogen bonded bis-urea supramolecular polymers. *J. Phys. Chem. B* **2013**, *117*, 5379−5386.

(26) Bochicchio, D.; Pavan, G. M. Effect of concentration on the supramolecular polymerization mechanism via implicit-solvent coarse-grained simulations of water-soluble 1, 3, 5−benzenetricarboxamide. *J. Phys. Chem. Lett.* **2017**, *8*, 3813−3819.

(27) Wang, J.; Wolf, R. M.; Caldwell, J. W.; Kollman, P. A.; Case, D. A. Development and testing of a general amber force field. *J. Comput. Chem.* **2004**, *25*, 1157−1174.

(28) De Jong, D. H.; Singh, G.; Bennett, W. D.; Arnarez, C.; Wassenaar, T. A.; Schafer, L. V.; Periole, X.; Tieleman, D. P.; Marrink, S. J. Improved parameters for the martini coarse-grained protein force field. *J. Chem. Theory Comput.* **2013**, *9*, 687−697.

(29) Yesylevskyy, S. O.; Schäfer, L. V.; Sengupta, D.; Marrink, S. J. Polarizable water model for the coarse-grained MARTINI force field. *PLoS Comput. Biol.* **2010**, *6*, No. e1000810.

(30) Stephens, P. J.; Devlin, F. J.; Chabalowski, C. F.; Frisch, M. J. *Ab initio* calculation of vibrational absorption and circular dichroism spectra using density functional force fields. *J. Phys. Chem.* **1994**, *98*, 11623−11627.

(31) Weigend, F.; Ahlrichs, R. Balanced basis sets of split valence, triple zeta valence and quadruple zeta valence quality for H to Rn: Design and assessment of accuracy. *Phys. Chem. Chem. Phys.* **2005**, *7*, 3297−3305.

(32) Grimme, S.; Ehrlich, S.; Goerigk, L. Effect of the damping function in dispersion corrected density functional theory. *J. Comput. Chem.* **2011**, *32*, 1456−1465.

(33) Frisch, M. J.; Trucks, G. W.; Schlegel, H. B.; Scuseria, G. E.; Robb, M. A.; Cheeseman, J. R.; Scalmani, G.; Barone, V.; Petersson, G. A.; Nakatsuji, H.; Li, X., et al. *Gaussian 16 Revision C.01*; Gaussian Inc.: Wallingford CT, 2016.

(34) Hehre, W. J. Ab initio molecular orbital theory. *Acc. Chem. Res.* **1976**, *9*, 399−406.

(35) Lee, C.; Yang, W.; Parr, R. G. Development of the Colle-Salvetti correlation-energy formula into a functional of the electron density. *Phys. Rev. B* **1988**, *37*, 785.

(36) Rappoport, D.; Furche, F. Property-optimized Gaussian basis sets for molecular response calculations. *J. Chem. Phys.* **2010**, *133*, 134105.

(37) Pritchard, B. P.; Altarawy, D.; Didier, B.; Gibson, T. D.; Windus, T. L. New basis set exchange: An open, up-to-date resource for the molecular sciences community. *J. Chem. Inf. Model.* **2019**, *59*, 4814−4820.

(38) Lu, T.; Chen, F. Multiwfn: A multifunctional wavefunction analyzer. *J. Comput. Chem.* **2012**, *33*, 580−592.

(39) Lu, T. A comprehensive electron wavefunction analysis toolbox for chemists, Multiwfn. *J. Chem. Phys.* **2024**, *161*, 082503.

(40) Perdew, J. P.; Burke, K.; Ernzerhof, M. Generalized gradient approximation made simple. *Phys. Rev. Lett.* **1996**, *77*, 3865.

(41) Grimme, S.; Antony, J.; Ehrlich, S.; Krieg, H. A consistent and accurate *ab initio* parametrization of density functional dispersion correction (DFT-D) for the 94 elements H-Pu. *J. Chem. Phys.* **2010**, *132*, 154104.

(42) VandeVondele, J.; Hutter, J. Gaussian basis sets for accurate calculations on molecular systems in gas and condensed phases. *J. Chem. Phys.* **2007**, *127*, 114105.

(43) Kühne, T. D.; Iannuzzi, M.; Del Ben, M.; Rybkin, V. V.; Seewald, P.; Stein, F.; Laino, T.; Khaliullin, R. Z.; Schütt, O.; Schiffmann, F.; et al. CP2K: An electronic structure and molecular dynamics software package-Quickstep: Efficient and accurate electronic structure calculations. *J. Chem. Phys.* **2020**, *152*, 194103.

(44) Krishnan, R.; Binkley, J. S.; Seeger, R.; Pople, J. A. Self-consistent molecular orbital methods. XX. A basis set for correlated wave functions. *J. Chem. Phys.* **1980**, *72*, 650−654.

(45) Abraham, M. J.; Murtola, T.; Schulz, R.; Páll, S.; Smith, J. C.; Hess, B.; Lindahl, E. GROMACS: High performance molecular simulations through multi-level parallelism from laptops to supercomputers. *SoftwareX* **2015**, *1*, 19−25.

(46) Bussi, G.; Donadio, D.; Parrinello, M. Canonical sampling through velocity rescaling. *J. Chem. Phys.* **2007**, *126*, 014101.

(47) Parrinello, M.; Rahman, A. Polymorphic transitions in single crystals: A new molecular dynamics method. *J. Appl. Phys.* **1981**, *52*, 7182−7190.

(48) Darden, T.; York, D.; Pedersen, L. Particle mesh Ewald: An Nlog(N) method for Ewald sums in large systems. *J. Chem. Phys.* **1993**, *98*, 10089−10092.

(49) Humphrey, W.; Dalke, A.; Schulten, K. VMD: visual molecular dynamics. *J. Mol. Graphics* **1996**, *14*, 33−38.

(50) Laio, A.; Parrinello, M. Escaping free-energy minima. *Proc. Natl. Acad. Sci. U. S. A.* **2002**, *99*, 12562−12566.

(51) Barducci, A.; Bussi, G.; Parrinello, M. Well-tempered metadynamics: a smoothly converging and tunable free-energy method. *Phys. Rev. Lett.* **2008**, *100*, 020603.

(52) Fiorin, G.; Klein, M. L.; Hénin, J. Using collective variables to drive molecular dynamics simulations. *Mol. Phys.* **2013**, *111*, 3345−3362.

(53) Krack, M. Pseudopotentials for H to Kr optimized for gradient-corrected exchange-correlation functionals. *Theor. Chem. Acc.* **2005**, *114*, 145−152.

(54) Lippert, G.; Hutter, J.; Parrinello, M. A hybrid Gaussian and plane wave density functional scheme. *Mol. Phys.* **1997**, *92*, 477−488.

(55) Frederix, P. W.; Ulijn, R. V.; Hunt, N. T.; Tuttle, T. Virtual screening for dipeptide aggregation: toward predictive tools for peptide self-assembly. *J. Phys. Chem. Lett.* **2011**, *2*, 2380−2384.

(56) Sasselli, I. R.; Coluzza, I. Assessment of the MARTINI 3 performance for short peptide self-assembly. *J. Chem. Theory Comput.* **2024**, *20*, 224−238.

(57) Marrink, S. J.; De Vries, A. H.; Mark, A. E. Coarse grained model for semiquantitative lipid simulations. *J. Phys. Chem. B* **2004**, *108*, 750−760.

(58) Marrink, S. J.; Risselada, H. J.; Yefimov, S.; Tieleman, D. P.; De Vries, A. H. The MARTINI force field: coarse grained model for biomolecular simulations. *J. Phys. Chem. B* **2007**, *111*, 7812−7824.

(59) Barducci, A.; Bonomi, M.; Parrinello, M. Metadynamics. *Wiley Interdiscip. Rev.:Comput. Mol. Sci.* **2011**, *1*, 826−843.

(60) Grimme, S.; Bannwarth, C.; Shushkov, P. A robust and accurate tight-binding quantum chemical method for structures, vibrational frequencies, and noncovalent interactions of large molecular systems parametrized for all spd-block elements (Z = 1−86). *J. Chem. Theory Comput.* **2017**, *13*, 1989−2009.

(61) Bannwarth, C.; Ehlert, S.; Grimme, S. GFN2-xTB-An accurate and broadly parametrized self-consistent tight-binding quantum chemical method with multipole electrostatics and density-dependent dispersion contributions. *J. Chem. Theory Comput.* **2019**, *15*, 1652−1671.

(62) Lu, T. *Molclus program, version 1.12*; 2025, http://www.keinsci.com/research/molclus.html, (accessed on Mar 15, 2025).

(63) Lu, T.; Chen, Q. Independent gradient model based on Hirshfeld partition: A new method for visual study of interactions in chemical systems. *J. Comput. Chem.* **2022**, *43*, 539−555.

(64) Emamian, S.; Lu, T.; Kruse, H.; Emamian, H. Exploring nature and predicting strength of hydrogen bonds: a correlation analysis between atoms-in-molecules descriptors, binding energies, and energy components of symmetry-adapted perturbation theory. *J. Comput. Chem.* **2019**, *40*, 2868−2881.

Supporting Information: Temperature-Dependent Structural Transition in Hydrogen-Bonded Supramolecular Polymers Using Coarse-Grained Simulations

Nengjie Cao,[†] Fengxiang Zhou,[†] Xianggui Zhou,[†] Jinyuan Mao,[†] Xiangmeng Jia,[†] and Jiajia Zhou*,[†,‡]

[†]*South China Advanced Institute for Soft Matter Science and Technology, School of Emergent Soft Matter, South China University of Technology, Guangzhou 510640, China*

[‡]*Guangdong Provincial Key Laboratory of Functional and Intelligent Hybrid Materials and Devices, South China University of Technology, Guangzhou 510640, China*

E-mail: zhouj2@scut.edu.cn

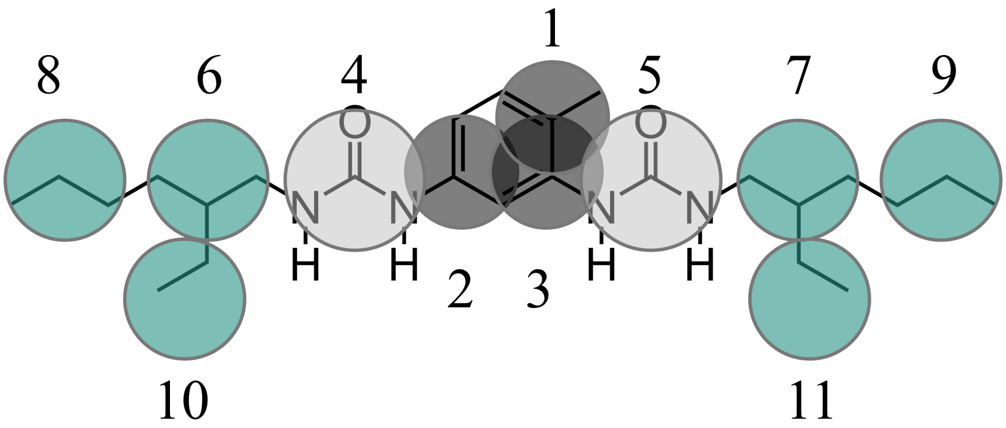

Figure S1. Atom-to-bead mapping of the EHUT.

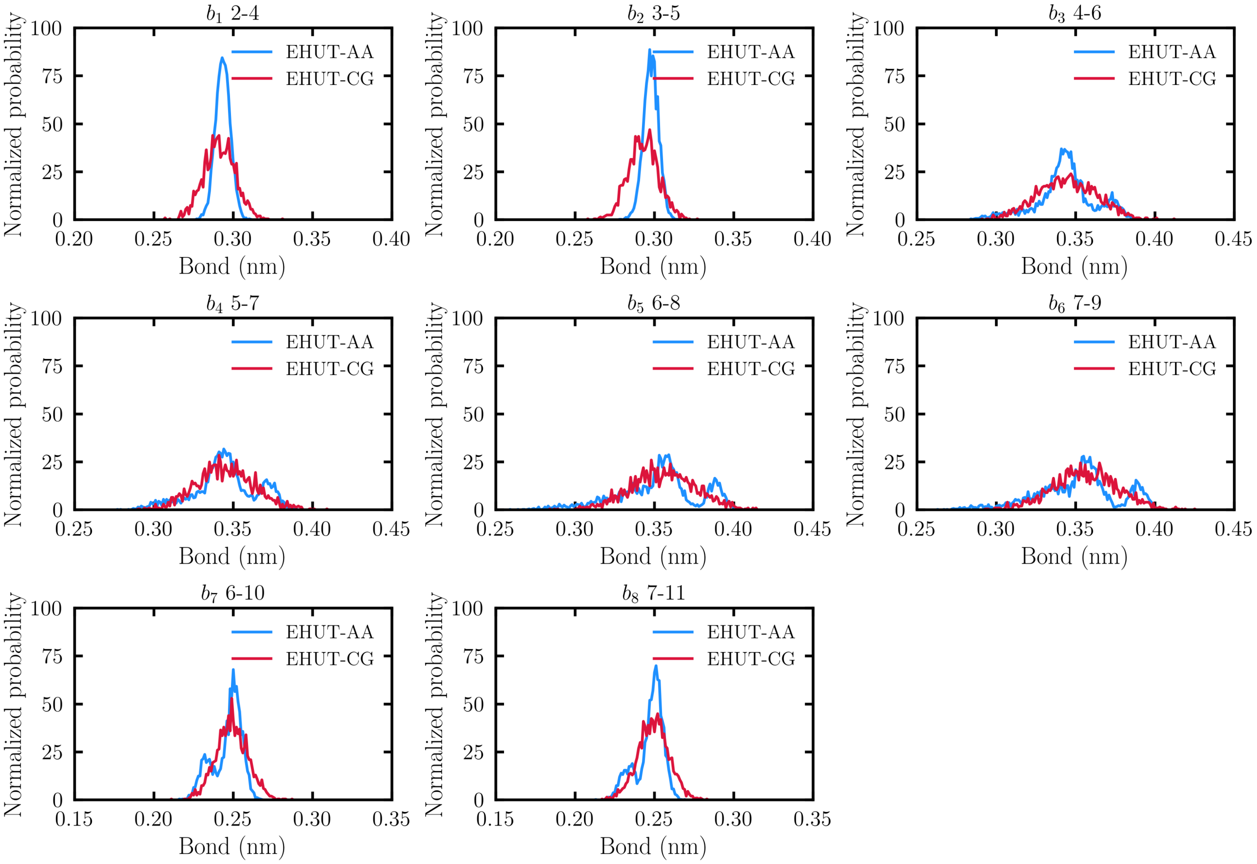

Figure S2. Averaged bond distribution of EHUT-AA (blue) and EHUT-CG (red) for different bonds.

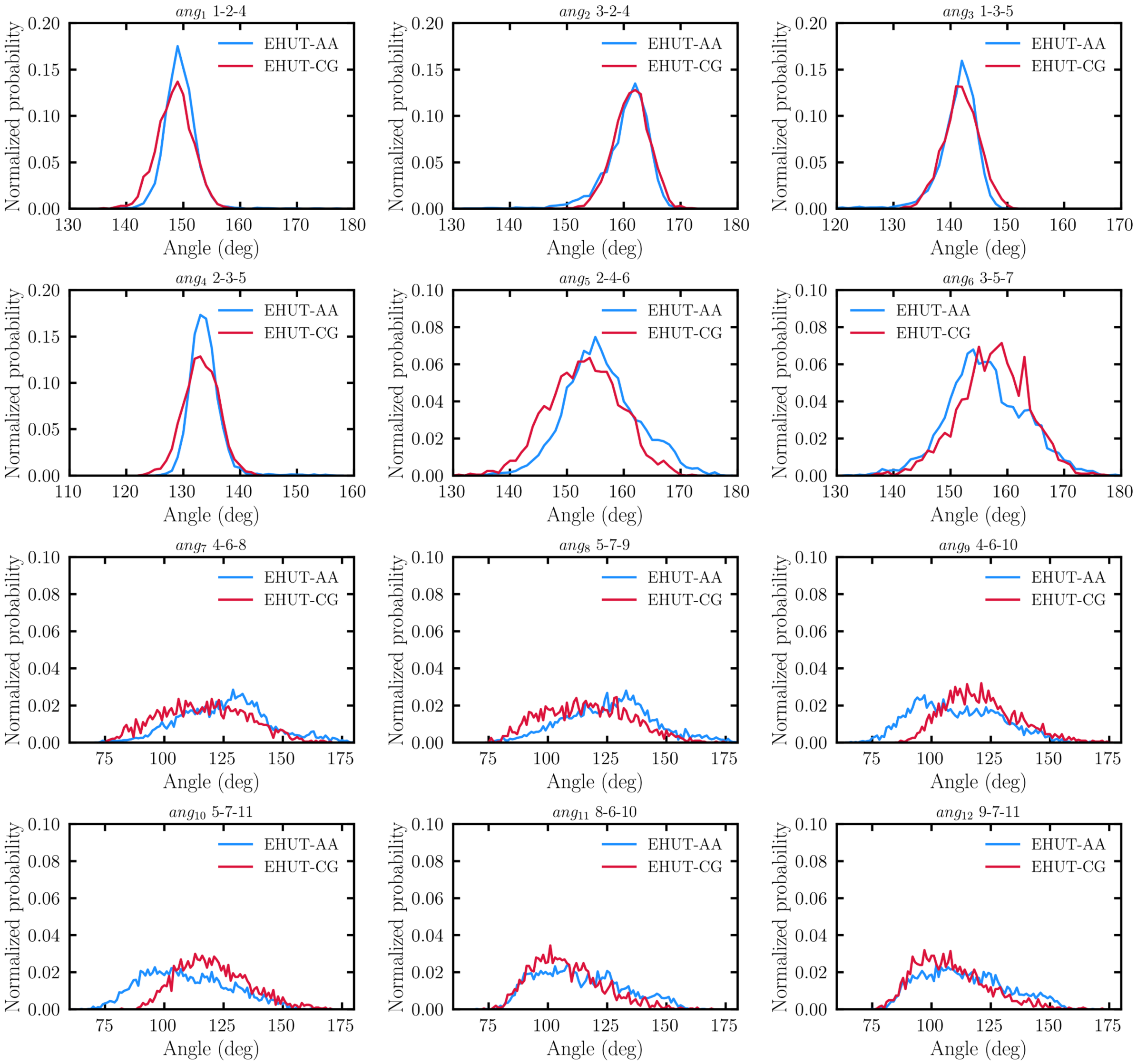

Figure S3. Averaged angle distribution of EHUT-AA (blue) and EHUT-CG (red) for different angles.

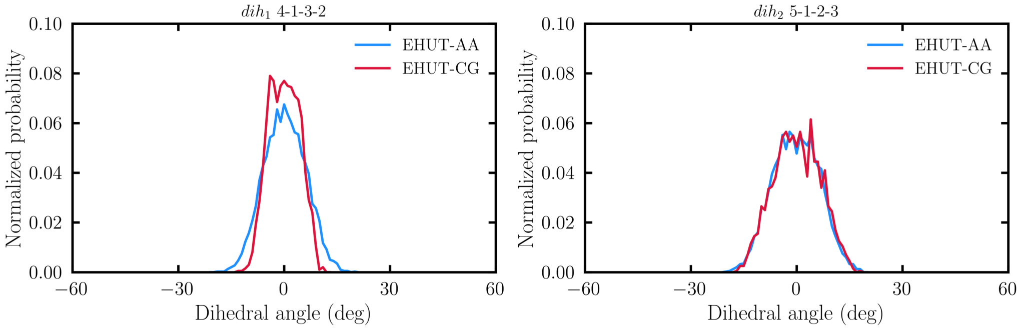

Figure S4. Averaged dihedral angle distribution of EHUT-AA (blue) and EHUT-CG (red) for different dihedral angles.

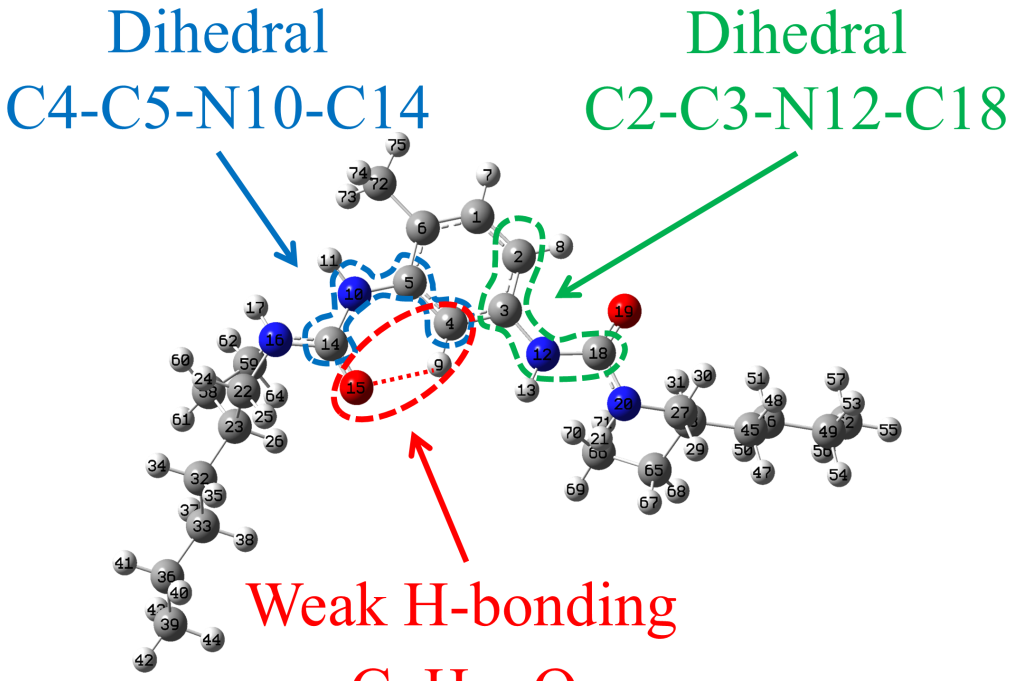

Figure S5. Schematic of the flexible potential energy surface scan of the EHUT molecule. The dihedral angles C4-C5-N10-C14 (blue) and C2-C3-N12-C18 (green) are the two scanned dihedrals. The red color indicates the C–H$\cdots$O weak hydrogen bond.

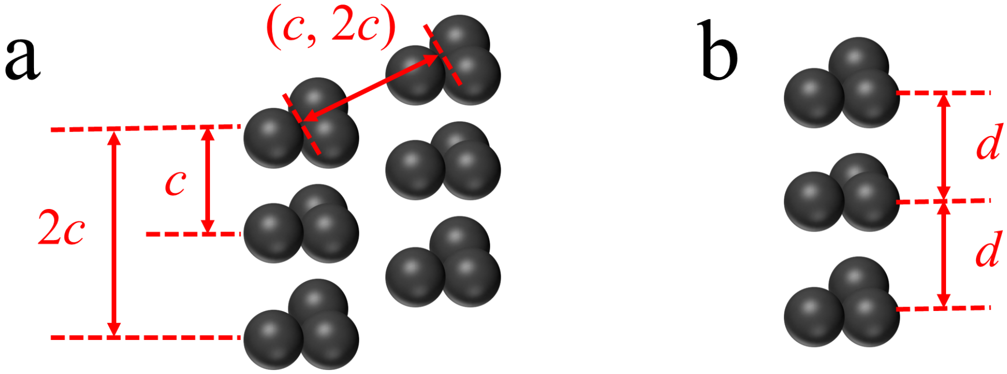

Figure S6. (a)Schematic of neighboring BTA cores for radial distribution functions $g(r)$ at stacking distance (c, closest neighbor; $2c$, second neighbor; etc.). Intercore spacing c equals 4.7 Å. The intercore distance between two filaments ranges between c and $2c$. (b) Schematic of neighboring BTA cores for order parameter Φ. Intercore spacing d equals 5.6 Å.

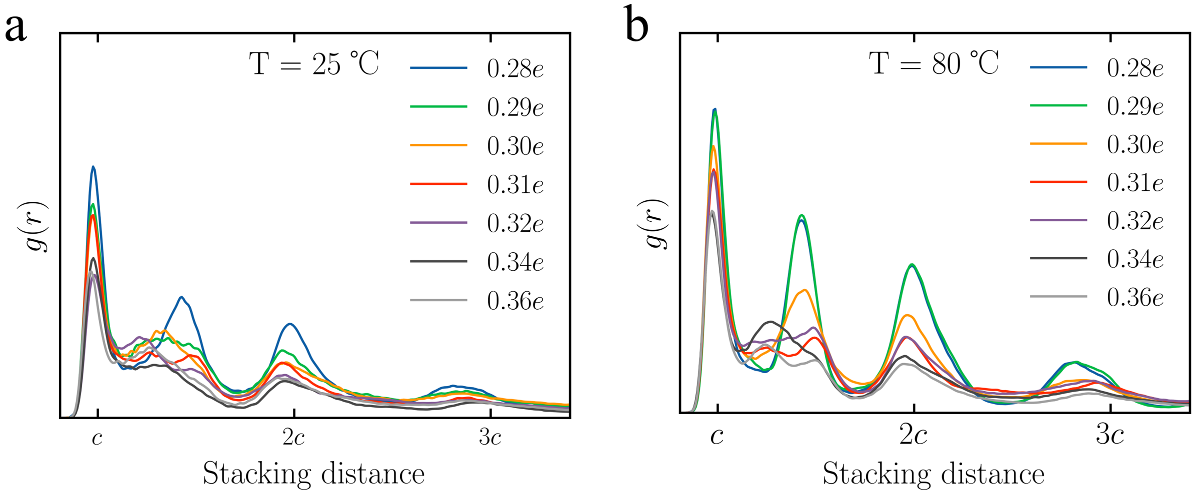

Figure S7. Amplification of stacking order in growing EHUT supramolecular polymers. Radial distribution functions $g(r)$ of EHUT cores in different charge q systems at (a) 25 °C and (b) 80 °C.

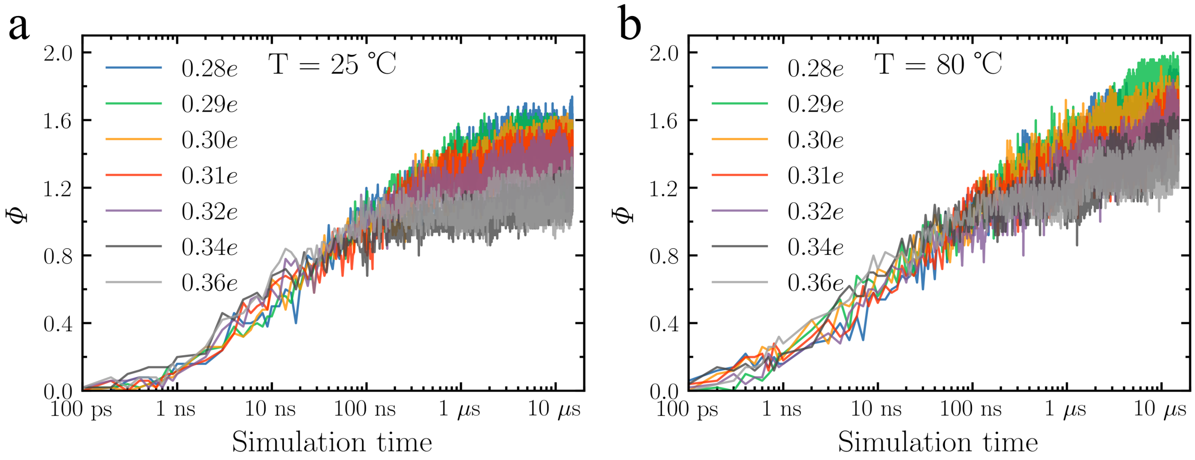

Figure S8. Order parameter Φ (core-core coordination) as a function of time for the EHUT-CG model at 20 g/L: (a) 25 °C and (b) 80 °C.

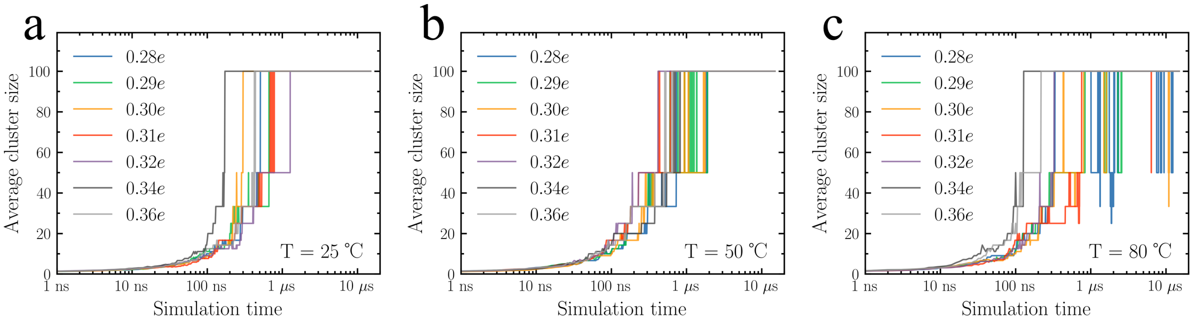

Figure S9. Average cluster size during EHUT-CG simulation for 100 self-assembling systems at (a) 25 °C, (b) 50 °C, and (c) 80 °C.

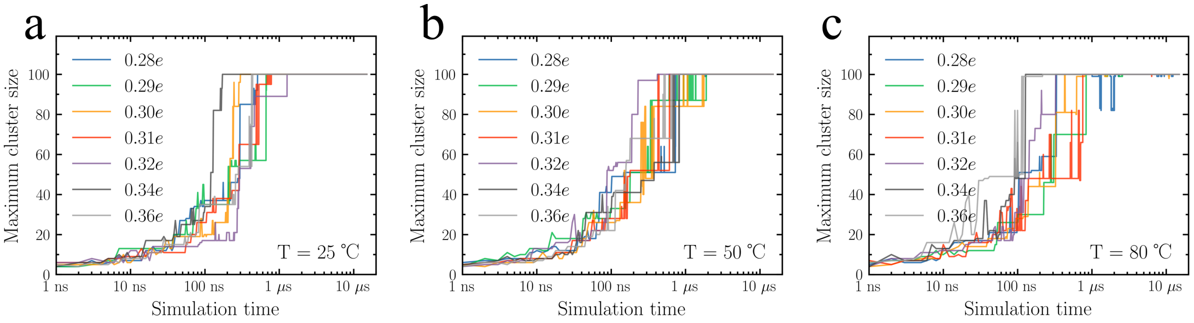

Figure S10. Maximum cluster size during EHUT-CG simulation for 100 self-assembling systems at (a) 25 °C, (b) 50 °C, and (c) 80 °C.

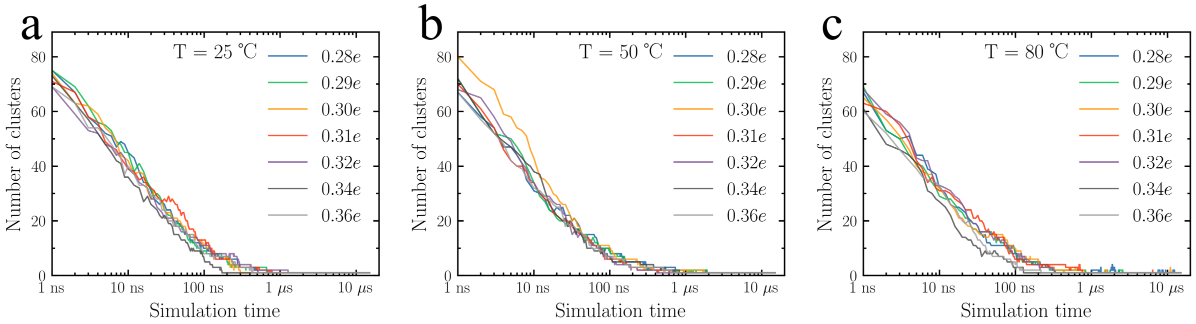

Figure S11. Number of clusters during EHUT-CG simulation for 100 self-assembling systems at (a) 25 °C, (b) 50 °C, and (c) 80 °C.

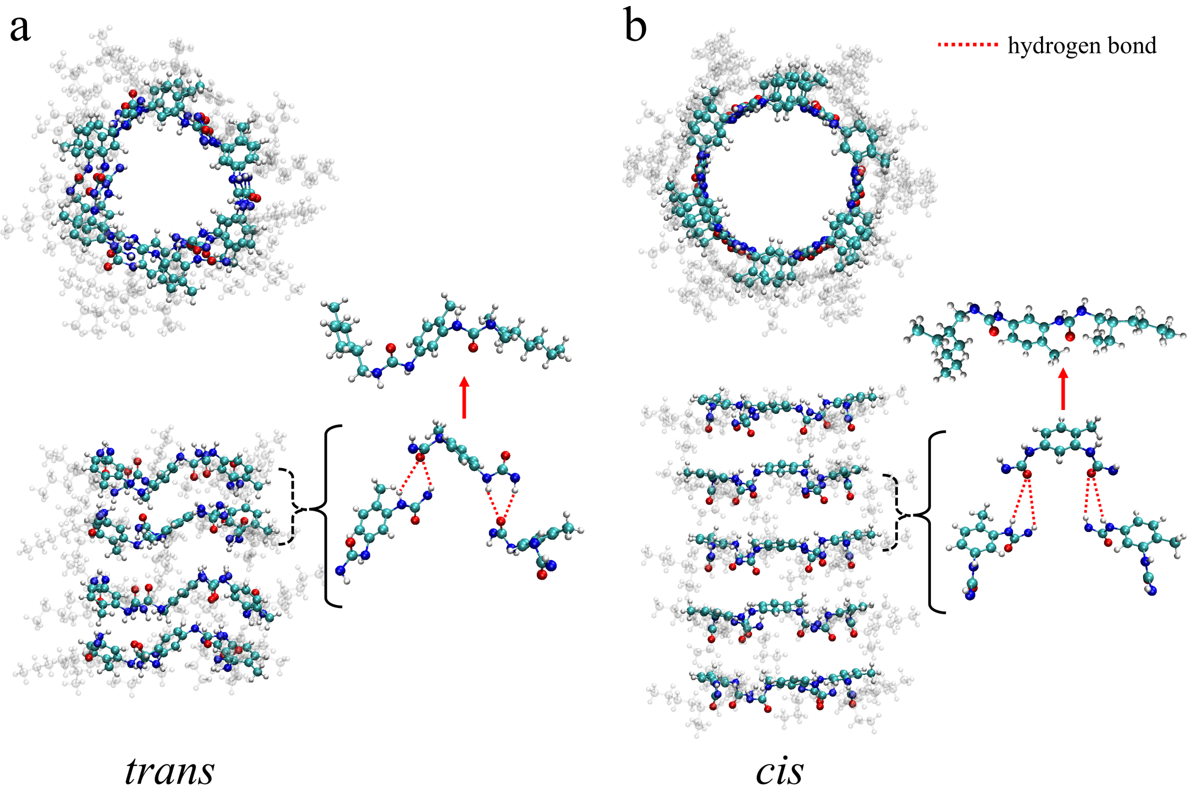

Figure S12. Proposed pre-assembled tube configurations of EHUT molecules based on experimental hypotheses: (a) *trans* and (b) *cis*. Each configuration is shown from the top-view (upper panels) and side-view (lower panels). Cyan, blue, red, and white beads represent C, N, O, and H atoms, respectively.

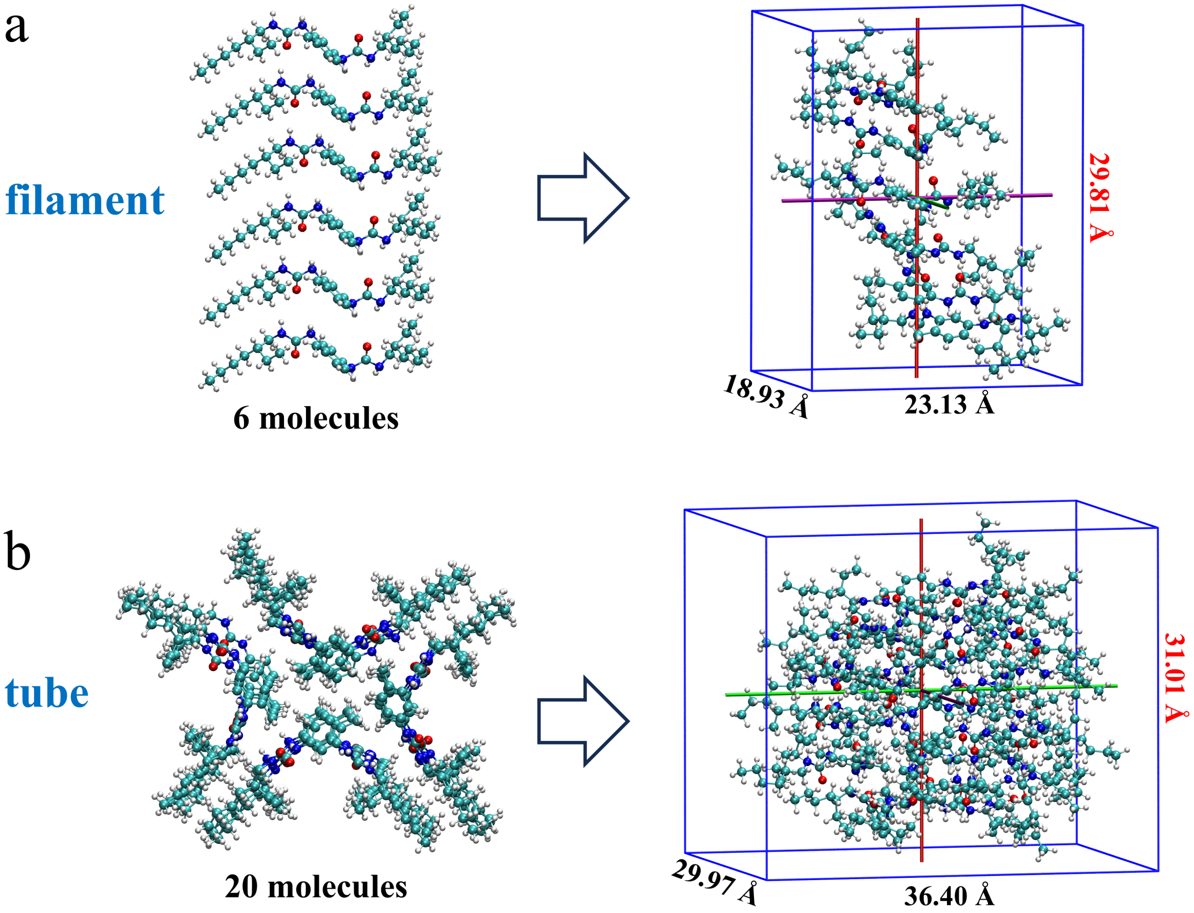

Figure S13. Schematic illustration of EHUT self-assemblies in ab initio molecular dynamics simulation (8 ps), showing the (a) filament and (b) tube structures. The red numbers indicate the characteristic lengths. The VDW surface is defined by the lengths of the three sides of the cube.